King's Research Portal

Document Version
Early version, also known as pre-print

[Link to publication record in King's Research Portal](#)

Silent T_1-Mapping Using the Variable Flip Angle Method with B_1 Correction

SCHOLARONE™
Manuscripts

1
2   plus1fillplus0.5fillplus0.5fillplus0.5fill
3
4   **FULL PAPER**
5
6
7
8
9   # Silent T_1-Mapping Using the Variable Flip Angle
10   # Method with B$_1$ Correction
11
12
13
14
15   **Emil Ljungberg**[1]* | **Tobias Wood**[1] | **Ana Beatriz**
16   **Solana**[2] | **Shannon Kolind**[3,4,5,6] | **Steven C.R. Williams**[1]
17 | **Florian Wiesinger**[†1,2] | **Gareth J. Barker**[†1]
18
19
20
21
22   [1]Department of Neuroimaging, Institute of
23   Psychology, Psychiatry & Neuroscience,
24   King's College London, London, UK
25   [2]ASL Europe, General Electric Healthcare,
26   Munich, Germany
27   [3]Department of Physics and Astronomy,
28   University of British Columbia, Vancouver
29   Canada
30   [4]Department of Radiology, University of
31   British Columbia, Vancouver, Canada
32   [5]International Collaboration on Repair
33   Discoveries, University of British Columbia,
34   Vancouver, Canada
35   [6]Medicine (Neurology), University of British
36   Columbia, Vancouver, Canada
37   [†]Authors contributed equally to this work

38   **Correspondence**
39   Emil Ljungberg, Department of
40   Neuroimaging, Institute of Psychiatry,
41   Psychology & Neuroscience, King's College
42   London, London, UK
43   Email: emil.ljungberg@kcl.ac.uk

44   **Present address**
45   *Centre for Neuroimaging Sciences,
46   Institute of Psychiatry (PO89), De
47   Crespigny Park, London SE5 8AF, United
48   Kingdom

Purpose: To compare the silent Rotating Ultra-Fast Imaging Sequence (RUFIS) to a traditional Cartesian gradient-echo acquisition scheme for Variable Flip-Angle (VFA) T_1-mapping.

Method: A two point VFA measurement was performed using RUFIS and Cartesian gradient echo in a quantitative phantom and healthy volunteers. To correct for B$_1$-errors, a novel Silent Magnetisation Prepared B$_1$-map Acquisition (SIMBA) was developed, which combined with RUFIS VFA allows for a completely silent T_1-mapping protocol.

Results: The silent protocol was found to have comparable repeatability but higher reproducibility *in-vivo* compared to the standard Cartesian protocol, and showed no increase in acoustic noise levels above background noise levels compared to a 30dB increase for the Cartesian acquisition.

Conclusion: VFA T_1-mapping using RUFIS is a feasible alternative to Cartesian gradient echo, achieving silent T_1-mapping with comparable acquisition time.

KEYWORDS
T_1, Quantitative, MRI, Silent, ZTE

1

1 | INTRODUCTION

The variable flip angle method (VFA), also referred to as DESPOT1, is a method for T_1 estimation, originally proposed by Christensen and later adapted for imaging by Fram [1, 2, 3, 4, 5]. To obtain a T_1 estimate, two or more fully-spoiled gradient-echo images are acquired with varying excitation flip angles and linearly fitted to the signal equation [6]. Due to the use of a gradient-echo sequence and the low number of acquisitions required, the VFA method is highly efficient compared to inversion-recovery based methods [7]. However, due to the large phase-encoding and spoiler gradients and short TR typically used in clinical protocols, the VFA method produces loud acoustic noise which is a drawback for patient comfort. In addition, at modern field strengths of 3T and above, B_1 inhomogeneity becomes a significant issue that must be corrected for with a separate acquisition.

In this work, we present a method for VFA T_1-mapping using the 3D **R**otating **U**ltra-**F**ast **I**maging **S**equence (RUFIS)[8], which presents several potential advantages over a traditional Cartesian acquisition. First, because of the centre-out radial k-space trajectory and gradual change of the gradient direction between subsequent excitations, the acquisition is almost completely silent [9]. Secondly, the RUFIS sequence achieves an effective echo time of zero (ZTE) by performing RF excitation with the readout gradients on and directly acquiring the free induction decay (FID)[10]. This extends the limit of T_1 quantification to tissues with very short T_2 such as bone and lung tissue, which often are considered to be MR-invisible [11, 12].

We present theoretical signal equations for RUFIS and analyse the constraints imposed on the acquisition by the ZTE readout. The theory and implementation of a novel silent B_1^+-mapping technique, using an extension to the double angle method with a RUFIS readout, is also presented. The proposed silent T_1 and B_1^+-mapping techniques, are demonstrated in a quantitative phantom with known relaxation characteristics and in vivo in four healthy volunteers, and compared to Cartesian methods. [12]

2 | METHOD

2.1 | Theory - Quantitative RUFIS

An outline of the RUFIS pulse sequence diagram is shown in figure 1a. Each spoke is a single FID readout with a centre-out trajectory in k-space. The magnitude of the applied gradients remains the same, while the relative strength along each axis changes the direction of the spoke in k-space. The k-space trajectory is designed such that the endpoints of the spokes trace a spiral on the surface of a sphere in k-space, resulting in a near silent acquisition [9]. Data acquisition starts as soon as the system has switched from transmit to receive mode, resulting in an effective echo time of zero (ZTE). To achieve this, only ultra-short hard RF pulses with low flip angles can be used with RUFIS. Further more, the TR in RUFIS is only limited by the readout duration since no time is required for slice/slab and phase encoding gradients.

When a steady state has been reached with RUFIS, the acquired signal will be equivalent to that of a spoiled gradient echo sequence, with the signal intensity depending on T_1 and proton density ρ, as well as the repetition time (TR), and flip angle (α) as

$$M_{z,spgr} = \rho \cdot \frac{1 - e^{-TR/T_1}}{1 - \cos(\alpha)e^{-TR/T_1}}. \tag{1}$$

With RUFIS, only short TRs and low flip angles are used, and therefore a first order approximation of (1) can be

made [13, 14] as

$$M_{z,spgr} = \frac{\rho}{1 + \frac{T_1}{TR} \cdot \frac{\alpha^2}{2}}. \tag{2}$$

This assumes that the signal is fully spoiled between repetitions. In RUFIS, this is achieved with RF spoiling as well as gradient spoiling from the readout gradients.

To perform a T_1-measurement using the variable flip angle method (VFA), a minimum of two flip angles are required. Spatial variations in the B_1^+ field has to be measured independently since changes in T_1 and α cannot be separated in the signal equation, as seen in (2). In RUFIS, there are two sources of B_1^+ variation; dielectric effects, and excitation profile effects. The former is here address through development of a novel B_1^+-mapping technique using RUFIS (described in the next section), and the latter through an analytical correction.

The non-uniform excitation profile in RUFIS is caused by the readout gradient being present during RF excitation[15]. For a given spoke, the gradients alter the resonant frequency across the sample parallel to the spoke direction, resulting in an unwanted sinc-shaped spatial variation of the flip angle in the direction of the spoke. The excitation profile is determined by the product of the duration of the RF pulse (τ_{rf}) and readout gradient magnitude G (which is inversely proportional to the readout bandwidth) as

$$B_1^+(\bar{r}) = \text{sinc}(\tau_{rf} \cdot \omega_G) \tag{3}$$

where $\omega_G = \bar{G} \cdot \bar{r}$ and $\bar{G}$ and $\bar{r}$ are vectors describing the current gradient direction and the position in the sample, and $\max|\omega_G| = rBW$, i.e. the readout bandwidth.

In order to achieve a flat excitation profile, hard RF pulses with the shortest possible duration should be used. This requires using the maximum possible RF amplitude and choosing the duration of the RF pulse to be that required to achieve the highest flip angle desired. This introduces a practical upper limit of the maximum flip-angle that can be achieved. Therefore, optimization of a RUFIS VFA T_1-mapping protocol has to consider a series of linked constraints. First, given a readout bandwidth the maximum excitation pulse width is limited to maintain an acceptable excitation profile; here we chose a limit of $\tau_{rf} \cdot rBW < 0.5$ which results in the excitation flip-angle at the edge of the FoV falling to 63% of the prescribed flip-angle. The chosen bandwidth will also determine the TR. The optimal flip angle sampling scheme in a VFA acquisition depends on the TR of the acquisition and the T_1 for which it is optimised [16]. With T_1 fixed, the optimal flip angles decrease with shorter TR. At the same time, a shorter TR, resulting from higher bandwidth, will also result in a shorter pulse width, and thus lower achievable flip angles. Tests on our scanner revealed that the pulse-width is the main limiting factor, and only at low bandwidths, here ± 7.8 kHz can flip angles close to the optimal be achieved. However, the flip angle limitations might be different for different MR systems as it depends on the RF amplifier, coils and SAR constraints.

2.2 | Theory - B_1^+-mapping with RUFIS

The proposed B_1^+ mapping method uses a composite preparation pulse with different flip angles prior to a RUFIS readout to saturate the magnetisation proportional to the total flip angle. We hereafter refer to this technique as SIMBA (**Si**lent **M**agnetisation prepared B_1^+ **A**cquisition). To enable magnetisation preparation, the RUFIS readout is divided into segments with N spokes per segment. A series of n RF pulses with the same phase, flip angle α_1, and short inter-pulse spacing are applied as a preparation, acting as one composite pulse with effective flip angle $n \cdot \alpha_1$. The transverse magnetisation after preparation is spoiled using a spoiling gradient, resulting in an initial longitudinal magnetisation

before readout given by $\tilde{M}_0 = \rho \cdot \cos(n\alpha_1)$. To produce a B_1^+-mapping technique that is consistent with the RUFIS readout, ultra-short RF pulses are used in the preparation. Using similar pulses in the preparation as in the readout enables characterization of potential errors in the RF pulse shape, which would result in a global, non-spatial, B_1^+ error.

The observed magnetisation in a RUFIS acquisition is proportional to the average magnetisation within a segment $\bar{M}_T(N)$ which can be expressed as

$$\bar{M}_T = \sin\alpha \cdot \bar{M}_z \tag{4}$$

$$\bar{M}_z = \tilde{M}_0 \cdot f + M_{z,spgr}(1-f) \tag{5}$$

$$f = \frac{\xi - \xi^{N+1}}{N(1-\xi)}, \quad \xi = \cos\alpha \cdot e^{-TR/T_1}. \tag{6}$$

where $\tilde{M}_0$ is the prepared longitudinal magnetisation at the beginning of the segment, and α is the excitation flip angle in the RUFIS readout. The full derivation of this expression can be found in the appendix. Encoding deviations in the B_1^+-field in the preparation as a factor λ, makes the transverse magnetisation proportional to λ as

$$\bar{M}_T = [\rho \cdot \cos(n \cdot \lambda \cdot \alpha_1) \cdot f + M_{z,spgr}(1-f)] \cdot \sin\alpha_0 \tag{7}$$

assuming full T_1 recovery between preparations. Figure 2a shows how the prepared magnetisation changes with the total preparation flip angle $(n \cdot \alpha_1)$ for $\lambda = (0.8, 1.0, 1.2)$. The repeated excitation in the RUFIS readout results in a positive offset in the signal, explained by the second term in (7), as shown in figure 2b. While increasing the number of spokes per segment will reduce the acquisition time, it will also reduce the dynamic range of the measurement.

(a)   (b)
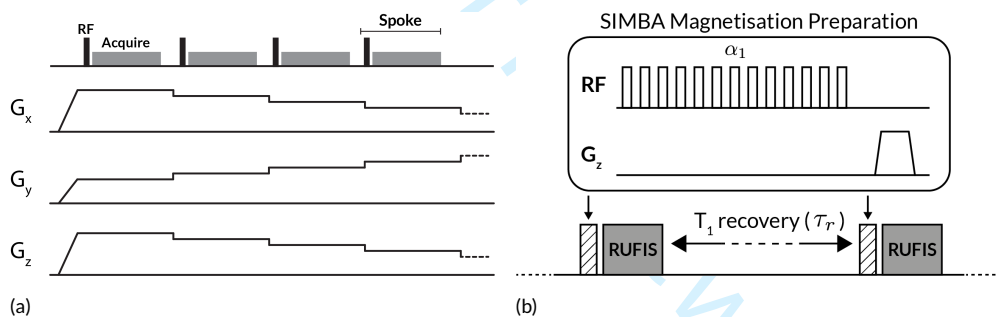
FIGURE 1 **(a)** Schematic pulse sequence diagram of the RUFIS sequence. Excitation is performed with an ultra-short hard RF pulse with the gradients on, and the free induction decay (FID) is acquired. The gradient magnitude stays the same and only the direction changes for each spoke. **(b)** Schematic of the SIMBA pulse sequence with the magnetisation preparation module before the RUFIS readout segment. A series of hard pulses with flip angle α_1 is applied and the transverse magnetisation after the train of pulses is crushed with a gradient on the z-axis. The delay τ_r between preparations allows for T_1 recovery.

2.3 | MR Acquisition

MR experiments were performed on a GE MR750 3T scanner (GE Healthcare, Chicago, IL) using the body coil for RF transmission and a 12-channel head RF receive coil. VFA T_1-mapping data were acquired with a 3D RUFIS sequence

(a)   (b)
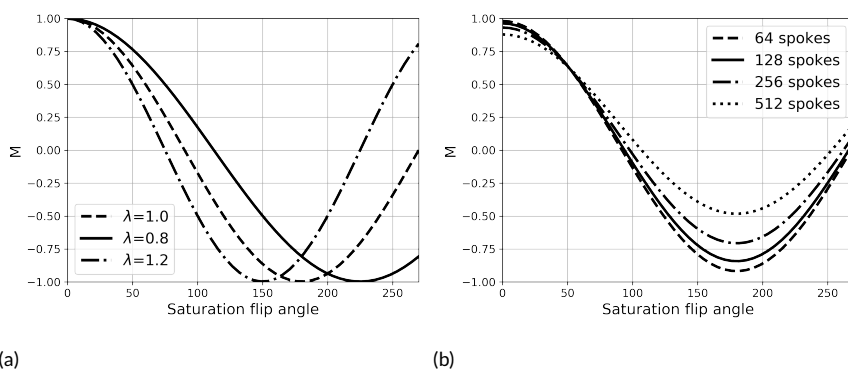
FIGURE 2 **(a)** Simulation showing the effect of B_1 variation (λ) on prepared magnetisation. **(b)** Simulation showing the effect of the RUFIS readout on the prepared magnetisation assuming $\lambda = 1, T_1 = 1s$, RUFIS FA=2° and TR=1 ms.

83 and a Cartesian SPGR sequence for comparison. The acquisitions were matched in field of view (FOV) (192x192x192
84 mm^3), voxel size (1.5x1.5x1.5 mm^3), and acquisition time ($\approx$4 min). Because of the difference in TR between RUFIS and
85 SPGR, a different set of flip angles (α) were acquired, to match the optimal set [16]. RUFIS data were acquired with
86 α=2° & 12°, TR=4.4 ms, TE=0 ms, readout bandwidth=$\pm$7.8 kHz, 24576 readout spokes in total. The RF pulse width
87 was fixed to 64 μs. The current implementation of the RUFIS sequence is restricted to a segmented readout, resulting in
88 an inter-segment spacing of about 20 ms. However, with a higher number spokes per segment, here 512, this delay does
89 not alter the steady state significantly. Cartesian images were collected with α=3.5°& 20°, TR=10.6 ms, TE=3.4 ms,
90 parallel imaging factor=1.5 (ASSET).

91   Two sets of B_1^+ maps were acquired; Bloch-Siegert [17] for correcting the SPGR data, and SIMBA for RUFIS data.
92 Bloch-Siegert data were acquired using a 2D multi-slice sequence with FA=15°, in-plane resolution=4x4 mm^2, slice
93 thickness=4 mm. SIMBA data were acquired using the 3D RUFIS sequence with readout bandwidth=$\pm$9.25 kHz, α=1°,
94 6x6x6mm^3 resolution, 256 spokes per segment, preparation α_1=5°, number of pulses in preparation train=[54,36,18,0],
95 3 s recovery time. Total acquisition time was 1 min. Each scanning session also included a sagittal T_1-weighted IR-
96 SPGR (BRAVO) for tissue segmentation with TE/TR/TI=3/7/400 ms, FOV=270x270x240 mm^3, slice thickness=1.2 mm,
97 in-plane resolution=1.05x1.05 mm^2, FA=11°, BW=31.25 kHz, and ASSET=1.75.

98   Four healthy volunteers were scanned twice with the same protocol, with an average time between scan sessions of
99 50 days (range: 48-52 days). In each session, the anatomical BRAVO image was acquired once and the VFA T_1-mapping
100 protocols using RUFIS and SPGR, with B_1^+ correction, were acquired twice (without repositioning). All scans were
101 collected under ethical approval by the Camberwell St Giles NHS (National Health Service) HRA (Health Research
102 Authority) Research Ethics Committee and participants gave written informed consent.

103   The protocol details above were also used to scan a quantitative phantom consisting of 12 vials with a range
104 of T_1 values (T_1=200-1500 ms, EUROSPIN test object 5 (TO5)[18]). Vials were mounted in an in-house made styro-
105 foam mount. Due to the small size of the vials ($\approx$2 cm in diameter), an additional SIMBA scan with higher resolution
106 (4x4x4mm^3) was acquired for the phantom experiment. Increasing the resolution also increased the TR to 1.6 ms which
107 was accounted for by reducing the number of spokes per segment to 176, to maintain the same T_1 recovery during the
108 readout.

109   Acoustic noise measurements were performed using a Casella (IDEAL Industries, Ill) CEL-63X sound meter with an
110 external microphone placed in the centre of the bore, mounted to a cylindrical water phantom with padding between

the phantom and microphone to avoid vibrations. Measurements were taken throughout each of the scans with a sampling rate of 1 sample every 2 s. Within a 40 s segment for each sequence, the average A-weighted equivalent sound level (LAEQ [dBA]) and C-weighted peak sound level (LCPEAK [dBC]) were calculated.

2.4 | Image Reconstruction and Processing

Data acquired with RUFIS were reconstructed offline in MATLAB (MathWorks, Natick, MA, USA). Radial k-space data were gridded using the Kaiser-Bessel method. Coil sensitivity maps were estimated using ESPIRiT, implemented in the Berkeley Advanced Reconstruction Toolbox (BART) [19, 20, 21]. Images were reconstructed using a SENSE reconstruction with 3D Total Variation regularization with $\lambda = 0.001$ implemented in the `pics` command in BART. For SIMBA data, coil sensitivity maps were estimated from the centre of k-space using the method described by McKenzie et al., also implemented in BART [22].

To calculate the SIMBA B_1^+-map, the data were mapped onto the real axis using the first image (no preparation pulses) as the reference. The B_1^+-map was then calculated through a non-linear fit of the real data to the following equation

$$M = A \cdot \cos(B_1 \cdot n \cdot \alpha) + C. \tag{8}$$

To correct for the excitation profile in the RUFIS acquisition, an iterative simulation was performed where the excitation profile for individual spokes was calculated analytically using equation (3). The 3D excitation profile was calculated for 1024 spokes and then averaged. The simulated excitation profile was then multiplied by the SIMBA B_1^+-map to obtain a total B_1^+-correction.

Data acquired with RUFIS and SPGR were motion corrected using mcFLIRT[23]. B_1^+-maps from SIMBA and Bloch-Siegert were registered and transformed to the space of the associated VFA acquisition using an affine transformation [24]. The transformed B_1^+-maps were smoothed using a Gaussian kernel with 8 mm FWHM to reduce propagation of noise into the T_1-maps. Quantitative T_1 and proton density maps were calculated using a linear fit, implemented in the QUantitative Imaging Tools (QUIT) [25]. The first RUFIS and SPGR acquisition within each scanning session were registered to the BRAVO scan using a combined affine and non-linear registration[26]. The second VFA acquisition of each scanning session was registered to the first VFA acquisition using an affine transformation. This transformation was then combined with the non-linear transformation to the BRAVO image.

To obtain unbiased regions of interest (ROI) for analysis of the T_1-maps, the BRAVO data for each subject and each visit were segmented using Freesurfer [27]. The following ROIs from the FreeSurfer analysis were used in the analysis: Pallidum (ID:13+52), Thalamus (ID:10+49), Caudate (ID:11+50), Putamen (ID:12+51), Corpus Callosum (CC) posterior (ID:255), CC anterior (ID:251), cerebral white matter (WM) (ID:2+41), cerebral cortex (ID:3+42). FreeSurfer ROIs were warped to the native space of the VFA data using the previously calculated transformations in a single step with MultiLabel interpolation [24]. Average T_1 values were calculated within each ROI, bilateral ROIs were averaged. The image analysis pipelines were developed using the `nipype` framework [28].

2.5 | Statistical Analysis

Repeated scans within the same session were treated as measurements performed under identical conditions, defined as repeatability conditions [29], and analysed using the methods described by Bland and Altman[30]. Within each visit, each sequence, and each ROI, the mean ($\bar{d}$) and standard deviation (s_d) of the difference between repeated scans across

the subjects were calculated, from which the limits of agreement (LoA) were calculated as LoA $= \bar{d} \pm 1.96 \cdot s_d$. The coefficient of repeatability (CoR) was calculated as $CoR_w = 2s_d$, with subscript w indicating within visit. The CoR is an aggregate measure of the absolute variability in the data, i.e. it does not scale with the true T_1 within the ROI. This gives complimentary information to that from the coefficient of variation (CoV), which is calculated per subject as $CoV_w = 100 \cdot \text{std}(y_1, y_1)/\text{mean}(y_1, y_2)$ where y_1 and y_2 are the test-retest T_1 values. The CoV is a percentage estimate, which is scaled by the true T_1 inside the ROI. CoR and average CoV will be reported here. Low CoR and CoV indicates high repeatability.

Repeated scans at the two different time points (i.e. visits), were treated as measurements taken under repro-ducibility conditions[29], with day-to-day biological variation and conditions in the scan room being factors not held constant. All other parameters were matched between the two scans. The within subject test-retest mean and differ-ence in T_1 were utilized for the reproducibility analysis. The average difference between the test-retest values at each time point (D) and the standard deviation (s_D) were calculated. The corrected standard deviation of the mean of the differences was calculated as $s_c = \sqrt{s_D^2 + \frac{1}{4}s_{d,1}^2 + \frac{1}{4}s_{d,2}^2}$[30], where $s_{d,1}$ and $s_{d,2}$ are the standard deviation of the test-retest differences at the two time points. The coefficient of reproducibility was calculated as $CoR_b = 2s_c$, and the coefficient of variability as $CoV_b = 100 \cdot \text{std}(y_1, y_1)/\text{mean}(y_1, y_2)$ where y_1 and y_2 are the average T_1 values for visit 1 and 2 for each subject. Subscript b here indicates between visits.

3 | RESULTS

3.1 | B_1^+-mapping with SIMBA

The calculated B_1^+ map from SIMBA is shown in figure 3 along with the Bloch-Siegert B_1^+-map for comparison. The B_1^+ maps have been transformed to VFA space and smoothed as previously described. In this example, the B_1^+ field estimated by SIMBA is lower than Bloch-Siegert, a pattern that was also observed in the other subjects and in the repeated scans. The simulated excitation profile in figure 3 shows that the average excitation profile results in an effective B_1^+ down to about 0.9 of the nominal B_1^+. Comparing RUFIS R_1-maps before and after B_1^+-correction using SIMBA and slice profile correction, also shown in figure 3, shows clear improvement.

3.2 | T_1-mapping

An overview of the T_1-maps and whole brain T_1 histograms calculated from the average of the two scans in the first visit from RUFIS, with SIMBA B_1^+ correction, and SPGR, with Bloch-Sieger B_1^+ correction, are presented in figure 4. Qualitatively, the T_1-maps from RUFIS looks very similar to Cartesian in the brain and the histograms also overlap to a great extent. One noticable difference between the two acquisitions is outside the brain. The ZTE readout in RUFIS captures the short T_2 signal from the skull which can be seen clearly in the proton density map and T_1 maps. The location of the WM peak in the T_1-histograms is similar between RUFIS and SPGR, with an average difference for the WM peak of $\Delta WM_{peak} = 68 \pm 41$ ms. However, a greater variability was observed for GM, $\Delta GM_{peak} = -179 \pm 74$ ms. This is also reflected in the Bland-Altman plot comparing T_1-values from RUFIS and SPGR within isolated ROIs presented in figure 5a, which shows larger difference for GM structures. Average T_1 values between the two repeated scans in the first visit, within isolated ROIs, are shown in table 1.

Similar results were observed in the phantom experiments. The RUFIS and Cartesian T_1-values were found to be highly correlated (Pearson's $\rho = 0.93$), but Bland-Altman analysis (figure 5b) showed a trend for larger differences in T_1 between the two sequences for longer T_1. The average difference was $\bar{d} = -0.39$ s with LoA=$(-1.22, 0.45)$s.
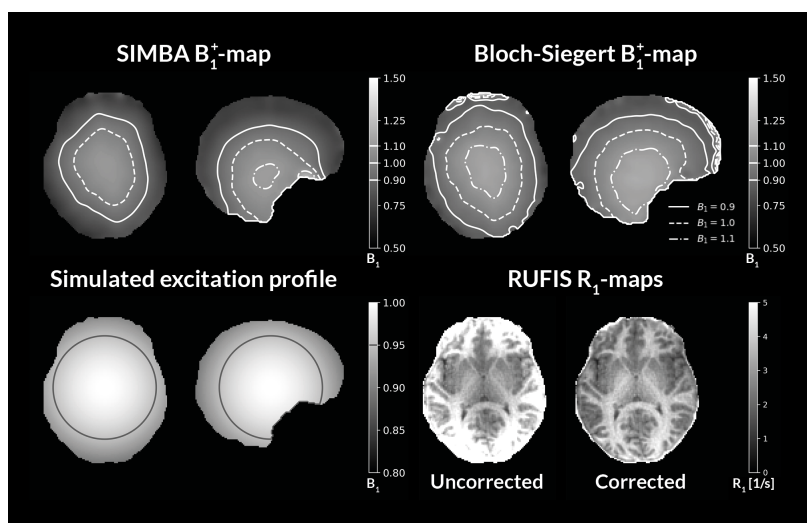
FIGURE 3 Top row: Comparison of B_1^+-maps acquired with SIMBA and Bloch-Siegert shift. SIMBA produces slightly lower B_1^+ values, as seen by the contour lines. Bottom row: Simulated slice profile correction for RUFIS and calculated RUFIS R_1 maps with and without B_1^+ correction using SIMBA and slice profile correction. The R_1 map is shown instead of T_1 as it better highlights the effects of the B_1^+ correction.

The within session average difference in T_1 in the phantom experiment, as calculated across all vials, was lower for SPGR ($\bar{d}_1 = -0.0046s, \bar{d}_2 - 0.0032s$) than RUFIS ($\bar{d}_1 = -0.018s, \bar{d}_2 = -0.0057s$). The limits of agreement (LoA) were comparable between SPGR (LoA$_1 = (-0.011, 0.0023)s$, LoA$_2 = (-0.014, 0.0076)s$) and RUFIS (LoA$_1 = (-0.040, 0.0037)s$, LoA$_2 = (-0.017, 0.0053)s$). Reproducibility analysis of the phantom data, calculated between the two visits across all vials, showed lower average difference with SPGR $\bar{D}_{SPGR} = -0.0008$ compared to RU-FIS $\bar{D}_{RUFIS} = -0.026$. However, there was a larger variability between the vials in the SPGR experiment, with LoA$_{SPGR} = (-0.14, 0.13)$ compared to RUFIS LoA$_{RUFIS} = (-0.092, 0.041)$.

Bland-Altman analysis of the in vivo data for each individual ROI reflects the results observed in the phantom data. The average within session repeatability for all ROIs for the two visits were comparable between the two sequence; RUFIS $CoR_{w,1} = 0.062/CoR_{w,2} = 0.024$, SPGR $CoR_{w,1} = 0.048/CoR_{w,2} = 0.082$. Better between sessions average reproducibility between all ROIs was found for RUFIS ($CoR_b = 0.066$) compared to SPGR ($CoR_b = 0.16$). Table 1 summarises the repeatability and reproducibility estimates from each individual ROI.
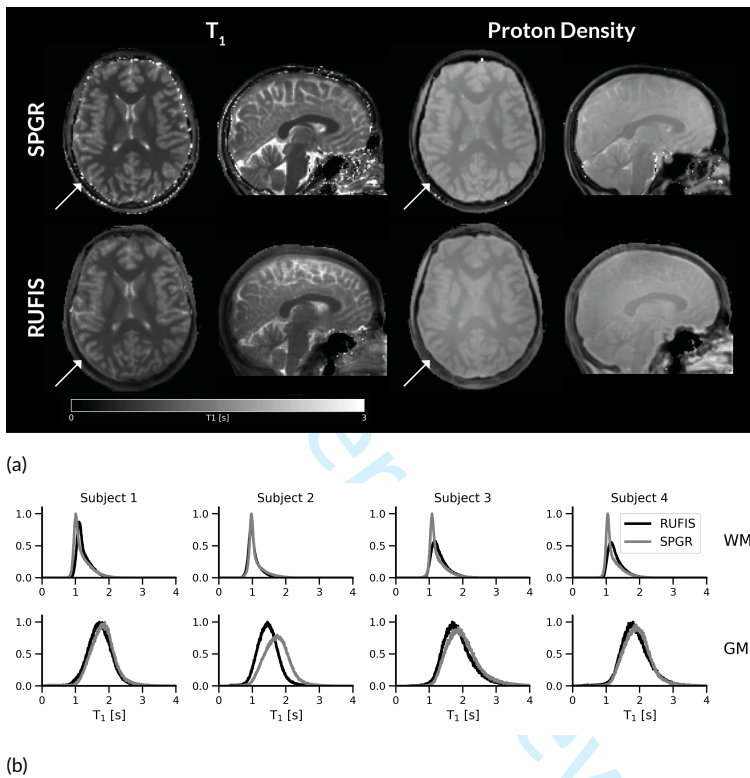
FIGURE 4 (a) Example of quantitative T_1 and proton density maps from one subject acquired with RUFIS and Cartesian SPGR. Due to the ZTE readout in RUFIS, a T_1 fit could be obtained in the cortical bone, indicated by the white arrows, and a higher proton density was observed in the same area. (b) T_1-histograms of whole brain white matter and cortical gray matter from all four subjects from the first visit, averaged over the two scans.

(a)

(b)
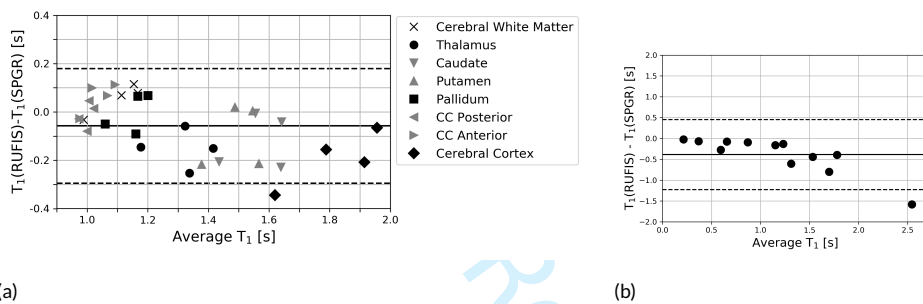
FIGURE 5 Bland Altman analysis comparing RUFIS and SPGR in vivo **(a)**, and in the EUROSPIN quantitative phantom **(b)**. Both in vivo and phantom experiment showed lower T_1 estimates from RUFIS for longer T_1.

TABLE 1 T_1 values in isolated ROIs averaged between the two scans in the first visit together with within session repeatability estimates (CoR_w & CoV_w) from the first visit and between sessions reproducibility measurements (CoR_b and CoV_b). Lower values of CoR and CoV are better. CoV are reported as mean$\pm\sigma$

	RUFIS					SPGR				
ROI	T_1[s]	$CoR_{w,1}$	$CoV_{w,1}$	CoR_b	CoV_b	T_1[s]	$CoR_{w,1}$	$CoV_{w,1}$	CoR_b	CoV_b
Cerebral WM	1.13±0.09	0.066	1.8±0.9	0.068	3±2	1.08±0.04	0.013	0.7±0.4	0.077	2±1
Thalamus	1.23±0.09	0.049	1.2±0.7	0.055	1.6±0.6	1.38±0.08	0.091	2±1	0.21	5±4
Caudate	1.5±0.1	0.063	1.2±0.7	0.093	1.9±0.4	1.63±0.08	0.054	1.0±0.4	0.24	5±3
Putamen	1.4±0.1	0.047	1.0±0.6	0.052	1.1±0.5	1.55±0.08	0.040	0.9±0.7	0.22	5±4
Pallidum	1.15±0.07	0.042	1.1±0.7	0.04	1.0±0.2	1.16±0.04	0.024	1.3±0.7	0.14	4±3
CC Posterior	0.99±0.03	0.045	1.5±0.9	0.045	1.2±0.4	1.01±0.03	0.041	2±1	0.14	4±2
CC Anterior	1.07±0.06	0.060	1.7±0.7	0.036	0.5±0.4	1.01±0.03	0.079	2±1	0.11	3±3
Cerebral Cortex	1.7±0.2	0.12	2±1	0.14	3±2	1.92±0.08	0.044	0.9±0.5	0.18	3±2
Mean	-	0.062	1.5±0.4	0.066	1.6±0.8	-	0.048	1.4±0.6	0.16	3.8±1

3.3 | Acoustic Noise Measurements

Table 2 shows average LAeq and LCpeak values from the acquisitions used in the protocol along with the ambient noise level in the scan room. RUFIS showed no measurable increase in sound pressure levels, but the sequence is in practice still just audible as it produces a higher pitched sound than the background noise (e.g. compressor pump) in the scan room. These measurement are comparable to those reported by Alibek et al., who measured a non-significant increase of 0.07 dB between RUFIS and ambient noise levels. Costagli et al. measured an increase of 2.5dBA for RUFIS compared to ambient noise levels, however, the ambient noise level in their scan room was 52.7 dBA which is much lower than what we measured. The increased acoustic noise during the SIMBA acquisition is due to the spoiling gradients after the preparation module.

TABLE 2 Summary of acoustic noise measurements from each sequence. Values are reported as mean$\pm\sigma$ noise levels over a 40 s period. The large standard deviation in the noise levels for SIMBA is due to the periodic spoiling gradients. (LAEQ - A-weighted equivalent continuous sound level, LCPEAK - C-weighted peak sound level)

Sequence	LAEQ [dBA]	LCPEAK [dBC]
Ambient	70.0 ± 0.2	89.7 ± 0.7
RUFIS	70.0 ± 0.2	89.6 ± 0.7
SIMBA	75.2 ± 4.0	102.5 ± 9.5
SPGR	103.3 ± 0.04	116.2 ± 0.1
Bloch-Siegert	98.8 ± 0.04	111.0 ± 0.1

4 | DISCUSSION

4.1 | Silent T_1-mapping

The acoustic noise produce by the MRI scanner during data acquisition is commonly reported by patients as one of the main unpleasant features of the scanning experience [32, 33]. In this work we have shown that the silent RUFIS sequence can be used for T_1-mapping together with a novel, silent, B_1^+-mapping method, SIMBA. We compared RUFIS to a Cartesian spoiled gradient echo acquisition and found that the two sequences produce comparable T_1 maps. The agreement between the two sequences was best in white matter, while in gray matter a longer T_1 was observed with the Cartesian acquisition. These results were also reflected in our phantom experiment. We found comparable in vivo repeatability between the two sequences, but reproducibility was better for RUIFS.

There are several differences in the data acquisition between the two sequences that could contribute to the observed difference in T_1. The signal equation used for VFA T_1-mapping assumes full spoiling of the transverse magnetisation before subsequent RF excitation. In the Cartesian sequence, spoiling was achieved by RF and separate gradient spoiling after the readout. In RUFIS, spoiling was mainly achieved using RF spoiling, together with some gradient spoiling from the readout gradients. Another difference is that RUFIS uses ultra-short hard RF pulses for excitation, compared to the shaped pulses used for slab-selective excitation in the Cartesian sequence. The excitation profile in RUFIS was corrected for using a first order correction. However, as the readout direction changes for each spoke, the effective flip-angle at any point in space, except isocentre, will change over time. A first order correction will make the effective flip-angle equal to the average flip-angle over time, and thus spin history effects are neglected.

224 The stronger excitation profile around the edges of the brain could contribute to the difference in T_1 in cortical GM
225 between the two sequence. However, we also see a difference in T_1 in deep GM structures, suggesting a non-spatial
226 phenomenon.

227 Various methods have been used for reducing the acoustic noise in MRI scanning, which broadly can be categorised
228 as; hardware modifications [34, 35] or pulse sequence modifications, mainly through soft gradient pulses [36, 37, 38, 39].
229 In contrast, the silent properties of RUFIS arise naturally from the gradient ordering of the sequence, and so performance
230 is not compromised. Previous studies have used RUFIS for silent imaging including T2-prepared fMRI [40], and structural
231 imaging at 3T [31] and 7T [9]. Another silent ZTE sequence is Looping Star which uses gradient echoes for T_2^* weighted
232 imaging [41]. Our acoustic noise measurement showed no measurable increase in the sound pressure levels during
233 RUFIS scanning compared to background noise levels, similar to Alibek et al. [31]. However, the quoted decibel values
234 will differ depending on the scan room environment and are not necessarily what the subject would experience inside
235 the scanner. The acoustic noise will also change depending on scan parameters such as the TR and number of spokes.
236 Nevertheless, we do not envisage any greater acoustic disturbance than measured herein.

237 While this study is the first to use the variable flip angle (VFA) method for T_1-mapping with RUFIS, there are
238 previous studies utilizing RUFIS for T_1-mapping using other techniques. Hsu and Lowe used RUFIS for 2D T_1-mapping
239 by acquiring multiple volumes during the transition to steady state [42]. Liu et al. have presented preliminary results
240 using RUFIS for T_1-mapping with inversion recovery and low-rank regularisation [43]. Their results look promising,
241 however only low spatial resolution (3x3x3mm^3) images were presented.

242 We chose to use a relatively low readout bandwidth (7.8 kHz) for the RUFIS acquisition in this study as our
243 sequence optimisation showed that this would enable the most optimal VFA flip angle sampling scheme. However, lower
244 bandwidths will widen the point spread function and increase chemical shift artefacts [44]. In a 3D radial acquisition,
245 chemical shift artefacts manifest in all three dimension as a spherical artefact. The chemical shift does not appear to
246 be a major issue in our study at 3T, but translating this technique to higher field strength will require higher readout
247 bandwidth. One benefit of the RUFIS acquisition is that changes in bandwidth is almost directly mirrored in the
248 acquisition time, since the TR only is limited by the readout duration. It is therefore possible to have two acquisition
249 with different readout bandwidths but increase the number of spokes to achieve the same acquisition time and thus
250 equivalent SNR. For a variable flip angle experiment however, increasing the bandwidth also reduces the maximum flip
251 angle.

4.2 | Silent B_1^+-mapping

253 T_1 mapping using VFA is inherently sensitive to errors in the B_1^+-map estimation. As shown by equation (2), and
254 previously by other authors, the apparent T_1 scales with the square of the flip angle bias field [13, 14]. It is therefore
255 likely that some of the variability in T_1 reported in the VFA literature can be attributed to B_1^+-errors, especially given
256 the large number of B_1^+-mapping techniques available. In this study, we chose to compare two complete protocols for
257 T_1-mapping including B_1^+-mapping. We chose to use the Bloch-Siegert method for B_1^+-correction of the Cartesian
258 SPGR data, as it is a standard sequence on the GE platform. This is not a silent sequence, however, and therefore we
259 developed a new methods for silent B_1^+-mapping (SIMBA), specifically designed for correction of RUFIS data. A train of
260 hard RF pulses was used for magnetisation saturation to match the RUFIS acquisition as closely as possible. SIMBA
261 could also be used with a single saturation pulse with different flip angle to match the excitation pulse in other sequences
262 as well.

263 It was outside the scope of the current work to provide a thorough comparison of Bloch-Siegert and SIMBA, but we
264 can draw some conclusions from our results. If there were discrepancies between the two B_1^+-mapping methods, then

this would result in differences in the T_1 estimation of brain structures that are located in the same area of the brain. However, in our data we observe a difference in T_1 in both deep and cortical GM but much smaller difference in WM, suggesting that other phenomena might be involved.

4.3 | Zero TE effects

One aspect of the RUFIS sequence that has not been studied in this work is the zero echo time (ZTE) readout, which results in sensitivity to short T_2 components, otherwise invisible to MR acquisitions [11, 12]. The ZTE effects can be observed in the T_1 and PD maps obtained with RUFIS, where a much higher proton density and better T_1 fit was observed in the cortical bone which has a very short T_1 and T_2, see white arrows in figure 4a. Recent works have suggested that the ultra short T_2-component from the myelin lipids are visible using ZTE and ultra short TE (UTE) acquisitions [45, 46]. However, the low bandwidth used in this work means that the signal from the solid myelin components will decay within the first few samples, and would, if anything, only contribute to an increased point spread function. Therefore, it is unlikely that the ZTE properties of RUFIS contribute to the observed differences in T_1 between RUFIS and SPGR.

5 | CONCLUSIONS

T_1-mapping with the variable flip angle method (VFA) using spoiled gradient echo imaging (SPGR) is a highly efficient method for T_1-mapping but requires an additional B_1^+-map for correction of the B_1^+-field. RUFIS is a zero TE, silent imaging sequence with a spoiled free induction decay (FID) readout which effectively can be used for quantitative imaging using the same signal equations as SPGR. In this work we have shown that RUFIS can be used for silent VFA T_1-mapping with results that are very similar to conventional Cartesian SPGR acquisition. A novel silent B_1^+-mapping technique based on RUFIS was also presented which can provide the necessary B_1^+ correction for VFA T_1-mapping using RUFIS.

We demonstrated a fully silent VFA T_1 and B_1^+-mapping protocol with higher reproducibility and comparable repeatability than the equivalent standard Cartesian sequence. Adoption of this protocol could lead to increased patient comfort in quantitative imaging studies.

297 **APPENDIX**

298 ## 5.1 | Derivation of the quantitative RUFIS signal equation

299 We begin from the results derived by Hsu and Lowe[42]. Let the longitudinal magnetisation of spoke n in segment m be
300 $M_z(n, m)$. With N spokes per segment we get

$$M_z(n, m) = M_z(0, m) \cdot \cos^n(\alpha)E_1 + \rho(1 - E_1) \cdot \frac{1 - \cos^n(\alpha)E_1^n}{1 - \cos(\alpha)E_1} \qquad (9)$$

301 where $E_1 = e^{-TR/T_1}$, α is the excitation flip angle, and ρ is the proton density. If $n \to \infty$ then $\cos^n(\alpha) \to 0$, and (9)
302 approaches the well known gradient echo steady state signal equation

$$\lim_{n \to \infty} M_z(n, m) = \rho \cdot \frac{1 - E_1}{1 - \cos(\alpha)E_1} = M_{z,spgr} \qquad (10)$$

303 To simplify (9), we set $\xi = \cos(\alpha)E_1$ and substitute in $M_{z,spgr}$ to obtain

$$M_z(n, m) = M_z(0, m) \cdot \xi^n + M_{z,spgr} \cdot (1 - \xi^n). \qquad (11)$$

304 With a segment of N spokes, the acquired magnetisation is proportional the average longitudinal magnetisation of all
305 spokes. This can be formulated as

$$\bar{M}_z(m) = \frac{1}{N}\sum_{i=1}^{N} M_z(i, m) = \frac{1}{N}\sum_{i=1}^{N}\left(M_z(0, m) \cdot \xi^i + M_{z,spgr} \cdot (1 - \xi^i)\right) = M_z(0, m) \cdot f + M_{z,spgr}(1 - f) \quad (12)$$

306 where

$$f = \sum_{i=1}^{N} \xi^i = \frac{\xi - \xi^{N+1}}{N(1 - \xi)} = \frac{\cos\alpha \cdot e^{-TR/T_1} - (\cos\alpha \cdot e^{-TR/T_1})^{N+1}}{N(1 - \cos\alpha \cdot e^{-TR/T_1})}. \qquad (13)$$

307 When data is collected in a steady state, the inter-segment delay (τ) will cause intermittent T_1-recovery. The
308 effect of this will depend on the number of spokes per segment as well as τ. The effect of this delay can be calculated
309 analytically. The magnetisation at the beginning of segment $m + 1$ is proportional to the magnetisation at the end of the
310 previous segment as well as the T_1-recovery between segments as

$$M_z(0, m + 1) = M_z(N, m) \cdot e^{-\tau/T_1} + \rho(1 - e^{-\tau/T_1}). \qquad (14)$$

311 Combining (14) with (11) yields

$$M_z(0, m + 1) = \left[M_z(0, m) \cdot \xi^N + M_{z,spgr} \cdot (1 - \xi^N)\right]e^{-\tau/T_1} + \rho(1 - e^{-\tau/T_1}). \qquad (15)$$

If the magnetisation at the beginning of each segment has reached a steady state ($\tilde{M}_0$) we can substitute $M_z(0, m + 1)$

and $M_z(0, m)$ with $\tilde{M}_0$ in (15) and solving for $\tilde{M}_0$ to get

$$\tilde{M}_0 = M_{z,spgr} \cdot \frac{e^{-\tau/T_1}(1 - \xi^N)}{1 - \xi^N e^{-\tau/T_1}} + \rho\frac{1 - e^{-\tau/T_1}}{1 - \xi^N e^{-\tau/T_1}}. \tag{16}$$

REFERENCES

[1] Christensen KA, Grant DM, Schulman EM, Walling C. Optimal determination of relaxation times of fourier transform nuclear magnetic resonance. Determination of spin-lattice relaxation times in chemically polarized species. The Journal of Physical Chemistry 1974;78(19):1971–1977. http://pubs.acs.org/doi/abs/10.1021/j100612a022.

[2] Gupta RK. A new look at the method of variable nutation angle for the measurement of spin-lattice relaxation times using fourier transform NMR. Journal of Magnetic Resonance 1977;25(1):231–235.

[3] Homer J, Beevers MS. Driven-equilibrium single-pulse observation of T1 relaxation. A reevaluation of a rapid "new" method for determining NMR spin-lattice relaxation times. Journal of Magnetic Resonance (1969) 1985;63(2):287–297.

[4] Fram EK, Herfkens RJ, Johnson GA, Glover GH, Karis JP, Shimakawa A, et al. Rapid calculation of T1 using variable flip angle gradient refocused imaging. Magnetic Resonance Imaging 1987;5(3):201–208.

[5] Deoni SCL. High-Resolution T1 Mapping of the Brain at 3T with Driven Equilibrium Single Pulse Observation of T1 with High-Speed Incorporation of RF Field Inhomogeneities (DESPOT1-HIFI). Journal of Magnetic Resonance Imaging 2007;26:1106–1111.

[6] Wang HZ, Riederer SJ, Lee JN. Optimizing the precision in T1 relaxation estimation using limited flip angles. Magnetic Resonance in Medicine 1987;5(5):399–416.

[7] Deoni SCL, Rutt BK, Peters TM. Rapid combined T1 and T2 mapping using gradient recalled acquisition in the steady state. Magnetic Resonance in Medicine 2003;49(3):515–526.

[8] Madio DP, Lowe IJ. Ultra-Fast Imaging Using Low Flip Angles and FIDs. Magnetic resonance in medicine 1995;34(4):525–529.

[9] Costagli M, Symms MR, Angeli L, Kelley DAC, Biagi L, Farnetani A, et al. Assessment of Silent T1-weighted head imaging at 7T. European Radiology 2016;26(6):1879–1888. http://dx.doi.org/10.1007/s00330-015-3954-2.

[10] Weiger M, Pruessmann KP. MRI with Zero Echo Time. eMagRes 2012;1:311–322.

[11] Wiesinger F, Sacolick LI, Menini A, Kaushik SS, Ahn S, Veit-Haibach P, et al. Zero TE MR bone imaging in the head. Magnetic Resonance in Medicine 2016;75(1):107–114.

[12] Gibiino F, Sacolick L, Menini A, Landini L, Wiesinger F. Free-breathing, zero-TE MR lung imaging. Magnetic Resonance Materials in Physics, Biology and Medicine 2015;28:207–215. http://dx.doi.org/10.1007/s10334-014-0459-y.

[13] Helms G, Finsterbusch J, Weiskopf N, Dechent P. Rapid radiofrequency field mapping in vivo using single-shot STEAM MRI. Magnetic Resonance in Medicine 2008;60(3):739–743.

[14] Baudrexel S, Reitz SC, Hof S, Gracien RM, Fleischer V, Zimmermann H, et al. Quantitative T1 and proton density mapping with direct calculation of radiofrequency coil transmit and receive profiles from two-point variable flip angle data. NMR in Biomedicine 2016;29(3):349–360.

[15] Grodzki DM, Jakob PM, Heismann B. Correcting slice selectivity in hard pulse sequences. Journal of Magnetic Resonance 2012;214:61–67. http://dx.doi.org/10.1016/j.jmr.2011.10.005.

[16] Wood TC. Improved formulas for the two optimum VFA flip-angles. Magnetic Resonance in Medicine 2015;74(1):1–3.

[17] Sacolick LI, Wiesinger F, Hancu I, Vogel MW. B1 mapping by Bloch-Siegert shift. Magnetic Resonance in Medicine 2010;63(5):1315–1322.

[18] Lerski RA, de Certaines JD. II. Performance assessment and quality control in MRI by Eurospin test objects and protocols. Magnetic Resonance Imaging 1993;11(6):817–833.

[19] Uecker M, Lai P, Murphy MJ, Virtue P, Elad M, Pauly JM, et al. ESPIRiT - An eigenvalue approach to autocalibrating parallel MRI: Where SENSE meets GRAPPA. Magnetic Resonance in Medicine 2014;71(3):990–1001.

[20] Uecker M, Tamir JI, BART Toolbox for Computational Magnetic Resonance Imaging; 2017. https://doi.org/10.5281/zenodo.1066014.

[21] Tamir J, Ong F, Cheng JY, Uecker M, Lustig M. Generalized Magnetic Resonance Image Reconstruction using The Berkeley Advanced Reconstruction Toolbox. In: ISMRM Workshop on Data Sampling and Image Reconstruction Sedona; 2016.
.

[22] McKenzie CA, Yeh EN, Ohliger MA, Price MD, Sodickson DK. Self-calibrating parallel imaging with automatic coil sensitivity extraction. Magnetic Resonance in Medicine 2002;47(3):529–538.

[23] Jenkinson M, Bannister P, Brady M, Smith S. Improved optimization for the robust and accurate linear registration and motion correction of brain images. NeuroImage 2002;17(2):825–841.

[24] Avants BB, Epstein CL, Grossman M, Gee JC. Symmetric diffeomorphic image registration with cross-correlation: Evaluating automated labeling of elderly and neurodegenerative brain. Medical Image Analysis 2008;12(1):26–41.

[25] Wood TC. QUIT: QUantitative Imaging Tools. Journal of Open Source Software 2017;3(26):656. https://github.com/spinicist/QUIT.

[26] Avants BB, Tustison NJ, Song G, Cook PA, Klein A, Gee JC. A reproducible evaluation of ANTs similarity metric performance in brain image registration. NeuroImage 2011 feb;54(3):2033–2044.

[27] Fischl B, Salat DH, Busa E, Albert M, Dieterich M, Haselgrove C, et al. Whole Brain Segmentation: Automated Labeling of Neuroanatomical Structures in the Human Brain. Neuron 2002;33(3):341–355.

[28] Gorgolewski K, Burns CD, Madison C, Clark D, Halchenko YO, Waskom ML, et al. Nipype: A Flexible, Lightweight and Extensible Neuroimaging Data Processing Framework in Python. Frontiers in Neuroinformatics 2011;5(August). http://journal.frontiersin.org/article/10.3389/fninf.2011.00013/abstract.

[29] Sullivan DC, Obuchowski NA, Kessler LG, Raunig DL, Gatsonis C, Huang EP, et al. Metrology Standards for Quantitative Imaging Biomarkers. Radiology 2015;277(3):813–825. http://pubs.rsna.org/doi/10.1148/radiol.2015142202.

[30] Bland JM, Altman DG. Statistical Methods for Assessing Agreement Between Two Methods of Clinical Measurement. Lancet 1986;327:307–310. http://www.sciencedirect.com/science/article/pii/S0140673686908378.

[31] Alibek S, Vogel M, Sun W, Winkler D, Baker CA, Burke M, et al. Acoustic noise reduction in MRI using Silent Scan: An initial experience. Diagnostic and Interventional Radiology 2014;20(4):360–363.

[32] MacKenzie R, Sims C, Owens RG, Dixon AK. Patients' perceptions of magnetic resonance imaging. Clinical radiology 1995;50(3):137–143.

[33] McNulty JP, McNulty S. Acoustic noise in magnetic resonance imaging: An ongoing issue. Radiography 2009;15(4):320–326. http://dx.doi.org/10.1016/j.radi.2009.01.001.

[34] Mansfield P, Glover PM, Beaumont J. Sound generation in gradient coil structures for MRI. Magnetic resonance in medicine : official journal of the Society of Magnetic Resonance in Medicine / Society of Magnetic Resonance in Medicine 1998;39(4):539–50. http://www.ncbi.nlm.nih.gov/pubmed/9543415.

[35] Edelstein Wa, Hedeen Ra, Mallozzi RP, El-Hamamsy SA, Ackermann Ra, Havens TJ. Making MRI quieter. Magnetic Resonance Imaging 2002;20:155–163.

[36] Hennel F, Girard F, Loenneker T. "Silent" MRI with soft gradient pulses. Magnetic Resonance in Medicine 1999;42:6–10. http://www.ncbi.nlm.nih.gov/pubmed/10398943.

[37] Hennel F. Fast spin echo and fast gradient echo MRI with low acoustic noise. Journal of magnetic resonance imaging : JMRI 2001;13(6):960–6. http://www.ncbi.nlm.nih.gov/pubmed/11382960.

[38] Schmitter S, Diesch E, Amann M, Kroll a, Moayer M, Schad LR. Silent echo-planar imaging for auditory FMRI. Magnetic Resonance Materials in Physics, Biology and Medicine 2008;21(5):317–325. http://www.ncbi.nlm.nih.gov/pubmed/18716815.

[39] Segbers M, Rizzo Sierra CV, Duifhuis H, Hoogduin JM. Shaping and timing gradient pulses to reduce MRI acoustic noise. Magnetic Resonance in Medicine 2010;64(2):546–53. http://www.ncbi.nlm.nih.gov/pubmed/20665798.

[40] Solana AB, Menini A, Sacolick LI, Hehn N, Wiesinger F. Quiet and Distortion-Free , Whole Brain BOLD fMRI Using T2 -Prepared RUFIS. Magnetic Resonance in Medicine 2016;75:1402–1412.

[41] Wiesinger F, Menini A, Solana AB. Looping Star. Magnetic Resonance in Medicine 2018;0(0):1–12.

[42] Hsu JJ, Lowe IJ. Spin-lattice relaxation and a fast T1-map acquisition method in MRI with transient-state magnetization. Journal of Magnetic Resonance 2004;169(2):270–278.

[43] Liu X, Gomez P, Sprenger T, Solana Sanchez AB, Wiesinger F, Menzel M, et al. Fast, Volumetric and Silent Multi-contrast Zero Echo Time Imaging. In: Proc. Intl. Soc. Mag. Reson. Med 25; 2017. p. 4035.

[44] Bydder M, Du J, Takahashi A, Shimakawa A, Hamilton G, Sinha S, et al. Chemical Shift Artifact in Center-Out Radial Sampling: A Potential Pitfall in Clinical Diagnosis. In: Proc. Intl. Soc. Mag. Reson. Med 15; 2007. p. 1811.

[45] Du J, Sheth V, He Q, Carl M, Chen J, Corey-bloom J, et al. Measurement of T1 of the Ultrashort T2* Components in White Matter of the Brain at 3T. PLoS ONE 2014;9(8).

[46] Boucneau T, Cao P, Tang S, Han M, Xu D, Henry RG, et al. In vivo characterization of brain ultrashort-T2 components. Magnetic Resonance in Medicine 2017;00(November):1–10. http://doi.wiley.com/10.1002/mrm.27037.